Photocatalytic CO_2 reduction integrated with biomass selective oxidation via single-atom Ru and P dual sites on carbon nitride

Zhendong Liu [a], Jiliang Ma [a,*], Yanzhu Guo [a], Min Hong [b,*], Runcang Sun [a,*]

[a] *Liaoning Key Lab of Lignocellulose Chemistry and BioMaterials, Liaoning Collaborative Innovation Center for Lignocellulosic Biorefinery, College of Light Industry and Chemical Engineering, Dalian Polytechnic University, Dalian 116034, China*
[b] *Centre for Future Materials & School of Engineering, University of Southern Queensland, Springfield Central, Queensland 4300, Australia*

ARTICLE INFO

ABSTRACT

Photocatalytic biorefinery integrated with CO_2 reduction to co-produce value-added chemicals and fuels is significant but challenging. Herein, a novel photocatalyst with dual active sites is constructed, in which Ru single atoms coordinated with N_2O_2 on phosphorus-doped carbon nitride ($Ru_1N_2O_2@PCN_x$) via a pre-assembled pyrolysis strategy. $Ru_1N_2O_2@PCN_{1.0}$ catalyst exhibits an exceptional performance in both CO_2 reduction and biorefinery processes, originating from the high photon-to-electron conversion rate. It achieves an extraordinary CO_2 reduction and biorefinery, with 100.1 $\mu mol\ g^{-1}\ h^{-1}$ evolution of CO and 91.2% yield of lactic acid. Furthermore, the as-prepared $Ru_1N_2O_2@PCN_{1.0}$ is successfully used in biomass-derived monosaccharides and xylan systems, validating the universality for broad applications. Experimental and theoretical analysis indicates that doping P in CN by replacing a corner C atom facilitates charge transfer/separation. Additionally, the introduction of $Ru-N_2O_2$ coordination regulates the electronic structure of CN and reduces the reaction energy barrier.

1. Introduction

The consumption of fossil fuels for the energy supply has caused a dramatic increase in atmospheric concentrations of CO_2, leading to severe global warming issues [1,2]. Atmospheric CO_2 levels are predicted to reach 590 ppm in 2100, with a global average temperature increase of 1.9 °C [3]. Therefore, research on CO_2 reduction by biocatalysis, electrocatalysis, or photocatalysis has been developed rapidly over the past decade [4–7]. Among them, CO_2 photoreduction is not only an ideal way to mitigate CO_2 emissions but also to convert CO_2 into valuable gaseous fuels and high-value-added chemicals. Recently, strategies for the photooxidation of natural organic waste (e.g., biomass) with simultaneous reduction of protons to produce high-value-added chemicals and hydrogen have been reported [8–10]. This photoconversion strategy usually involves a semiconductor material that absorbs light to excite electrons for proton reduction to hydrogen, while holes are utilized to oxidize the biomass to give high-value-added chemicals. Biomass photoreforming could also be combined with an analogous photoreduction of CO_2 [8,10]. However, the CO_2 reduction reaction involves the process of multiple electrons and protons transfer, leading to complex reaction pathways and kinetics [11,12]. Thus, the design of efficient and highly selective semiconductor-based photocatalysts for biorefineries integrated with CO_2 reduction reactions is desirable but still challenging.

Recently, single-atom catalysts, which incorporate the merits of both homogeneous and heterogeneous catalysts to offer novel concepts for enhancing photocatalytic activity, have attracted widespread interest [13,14]. Functional single-atom catalysts have been developed for photocatalytic hydrogen evolution, CO_2 reduction, hydrogen peroxide generation, organic contaminants degradation, and biorefinery [9, 15–18], with advantages of high selectivity, maximum metal atom utilization, and low reaction energy barriers. However, the high surface free energy caused by their ultra-small size makes it challenging to synthesize single-atom catalysts [19]. Furthermore, the high reactivity during synthesis and catalysis can lead to the aggregation of metals into nanoclusters and even nanoparticles, which will limit the large-scale application of single-atom catalysts. An effective strategy to overcome aggregation is the introduction of suitable carrier materials to anchor and stabilize the metal atoms.

Polymeric carbon nitride (CN), due to the ultra-high content of N atoms and good capability of coordination, is a suitable carrier for loading and stabilizing individual metal atoms [20–22]. Meanwhile, the lone pair electrons of N atoms motivate the coordination with metal

---

atoms, resulting in the majority of metal atoms coordinating with N to form M-N_x (M: metal atom) single catalysts [16,23,24]. For instance, Chen et al. reported the efficient and selective photocatalytic CO_2 reduction on CN by a single-atom La-N charge-transfer bridge, with a CO yield and selectivity of 92 μmol g^{-1} h^{-1} and 80.3%, respectively [23]. Hu et al. designed single-atom Pt-N bridges on CN for high-efficiency light-driven water splitting, in which the hydrogen evolution rate is ~94.0 times higher than that of pristine CN [24]. However, the reported CN-based photocatalysts with metal atoms are still plagued by the issues of inadequate catalytic sites, insufficient optical absorption capacity and low charge separation efficiency. Alternatively, the introduction of non-metallic atoms (e.g. P) into the CN not only increases the catalytic site but also adjusts the energy band structure of CN, providing a new handle to solve the above problem [25–27]. For example, Li and co-workers prepared bilayer thin CN nanosheets doped with non-metallic P elements and single-atom Co, and the formation of Co_1-N_4 and P-N coordination synergistically improved the transfer of electrons in CN, thereby facilitating the hydrogen evolution reaction [25]. Furthermore, single Cu atoms in P-doped CN with Cu_1N_3 coordination structures achieved a selective reduction of CO_2 to CO [27]. The visible light absorption capacity and photo-generated charge carrier separation efficiency of Cu_1N_3@CN were improved after P doping. Thus, we aim to design a novel photocatalyst comprising of Ru and P dual sites anchored on CN-based materials. This catalyst was then used in photocatalytic biorefineries coupling with CO_2 reduction to co-produce high value-added chemicals and gaseous fuels.

Herein, the dual active moieties of Ru-N_2O_2 and P-N on CN nanosheets ($Ru_1N_2O_2$@PCN_x) were successfully engineered for biorefineries coupling with CO_2 reduction to co-produce lactic acid and CO. $Ru_1N_2O_2$@$PCN_{1.0}$ has excellent photocatalytic activity in CO_2 reduction coupling with biomass conversion. Furthermore, the $Ru_1N_2O_2$@$PCN_{1.0}$ has excellent universality and is successfully used in biomass-derived monosaccharides and xylan systems. Experimental analysis coupled with density functional theory (DFT) simulations reveal that the presence of P in $Ru_1N_2O_2$@$PCN_{1.0}$ facilitates electron transport, while Ru-N_2O_2 coordination plays a crucial role in narrowing the band gap of CN and reducing the reaction energy barrier. Finally, a possible reaction mechanism for synchronous photocatalytic CO_2 reduction and biomass conversion in one system was presented.

2. Experimental section

2.1. Preparation of CN

To prepare pristine CN, 5.0 g of dicyandiamide was placed in a porcelain boat and then calcinated at 600 °C for 2 h under Ar flowing (99.99%, 50 mL min^{-1}). The temperature grew up with a ramping rate of 10 °C min^{-1}.

2.2. Preparation of $Ru_1N_2O_2$@PCN_x, PCN and $Ru_1N_2O_2$@$CN_{1.0}$

In a typical procedure, sodium hypophosphite (2.25 g) and dicyandiamide (5.0 g) were mixed in deionized water (6.0 mL) with constant stirring. Meanwhile, a certain volume (0.1, 0.5, 1.0, 2.0 or 3.0 mL) of $RuCl_3$ solution (20 mg mL^{-1}) was injected into the mixed solution drop by drop. Afterwards, the mixed solution was heated at 90 °C until the water was completely vaporized. The evaporated solid was conducted at 600 °C for 2 h under Ar atmosphere (99.99%, 50 mL min^{-1}) in a tubular furnace with a heating rate of 10 °C min^{-1}. The obtained solid was ground and washed with deionized water and anhydrous ethanol for several times, and then dried at 80 °C. According to the volume of $RuCl_3$ solution, the materials were denoted as $Ru_1N_2O_2$@PCN_x (x = 0.1, 0.5, 1.0, 2.0, 3.0). PCN was obtained using the same procedures without the addition of $RuCl_3$ solution as that of $Ru_1N_2O_2$@PCN_x. For $Ru_1N_2O_2$@$CN_{1.0}$, the procedure was similar to that of $Ru_1N_2O_2$@$PCN_{1.0}$, except that no sodium hypophosphite was added.

2.3. Photocatalytic activity tests

Typically, a certain amount of catalyst (CN, PCN, $Ru_1N_2O_2$@$CN_{1.0}$, or $Ru_1N_2O_2$@PCN_x) and 150 mg of biomass-derived feedstocks (e.g., mannose, fructose, glucose, rhamnose, arabinose, xylose, and xylan) were added into 30 mL solutions (e.g., KOH, HCl, H_2O), respectively. Subsequently, the mixture was transferred to the flat-bottom quartz reactor and degassed with CO_2 (110 kPa, 99.99%) for 5 times. After a period of stirring, the reactors were then illuminated with a 10 W Vlight lamp at 30 °C. Finally, the liquid and gas products were analyzed using high-performance liquid chromatography (HPLC) and gas chromatography (GC), respectively.

2.4. Poisoning experiments

10 mg of $Ru_1N_2O_2$@$PCN_{1.0}$, 150 mg of xylose, and 0.02 mol of different scavengers were added into 30 mL of KOH solution (1.0 M). Afterwards, the obtained reactors were degassed and charged with CO_2 (110 kPa, 99.99%) for 5 times. Then, the reactors were illuminated (Vlight lamp, 10 W) for 8 h at 30 °C. Finally, the detection methods of the samples are the same as above.

2.5. Recycling tests

Typically, a mixture of $Ru_1N_2O_2$@$PCN_{1.0}$ (10 mg), xylose (150 mg) and KOH solution (30 mL, 1.0 M) was added into the flat-bottom quartz reactor, in which was then charged with 110 kPa of CO_2 (99.99%). After that, the reactor was irradiated by Vlight lamp (10 W) for 8 h at 30 °C. Finally, the $Ru_1N_2O_2$@$PCN_{1.0}$ was filtrated, washed, dried, and then directly used for the next cycle.

2.6. Isotope-labeling tests

The test procedure for the $^{13}CO_2$ isotope experiment was the same as that for the standard photocatalytic biomass refining and CO_2 reduction test, except that $^{12}CO_2$ was replaced with $^{13}CO_2$ and the gas products were analyzed by the GC-MS and C NMR.

3. Results and discussion

3.1. Synthesis and morphological characterization of $Ru_1N_2O_2$@PCN_x

The preparation of $Ru_1N_2O_2$@PCN_x photocatalyst is schematically demonstrated in Fig. 1a. Initially, dicyandiamide, sodium hypophosphite, and ruthenium salt ($RuCl_3·xH_2O$) were mixed in deionized water and then evaporated at 90 °C to form a hybrid. Then, the hybrid was treated in the Ar atmosphere at 600 °C for 2 h to produce $Ru_1N_2O_2$@PCN_x photocatalyst. As shown in Figs. 1b, c and S1, scanning electron microscopy (SEM) images reveal that $Ru_1N_2O_2$@$PCN_{1.0}$ and CN present sheet-stacked and bulk structures, respectively. Energy dispersive spectrometry (EDS) mappings indicated that C, N, Ru, O, and P were uniformly distributed in $Ru_1N_2O_2$@$PCN_{1.0}$ (Fig. 1d-h). Similarly, transmission electron microscopy (TEM) images also showed a layered structure in $Ru_1N_2O_2$@$PCN_{1.0}$ without notable Ru nanoparticles (Fig. 1i-j), suggesting that Ru elements were successfully doped into the matrix to form single atoms. To further prove this, high-angle annular dark-field scanning transmission electron microscopy (HAADF-STEM) was employed. High-density isolated bright spots were observed on $Ru_1N_2O_2$@$PCN_{1.0}$, which were attributed to the Ru single atoms (Fig. 1k). To investigate the dispersion of Ru sites at the atomic level, electron energy-loss spectroscopy (EELS) was employed. As shown in Fig. S2, in the EELS spectra of the bright spots (indicated by square box), Ru, N, and O elements can be identified. The coexistence of N, O, and the single atom Ru in this region provides strong evidence for a Ru-N/O coordination structure [28,29]. The actual content of Ru single atoms in $Ru_1N_2O_2$@$PCN_{1.0}$ was detected to be 0.60 wt% by an inductively coupled
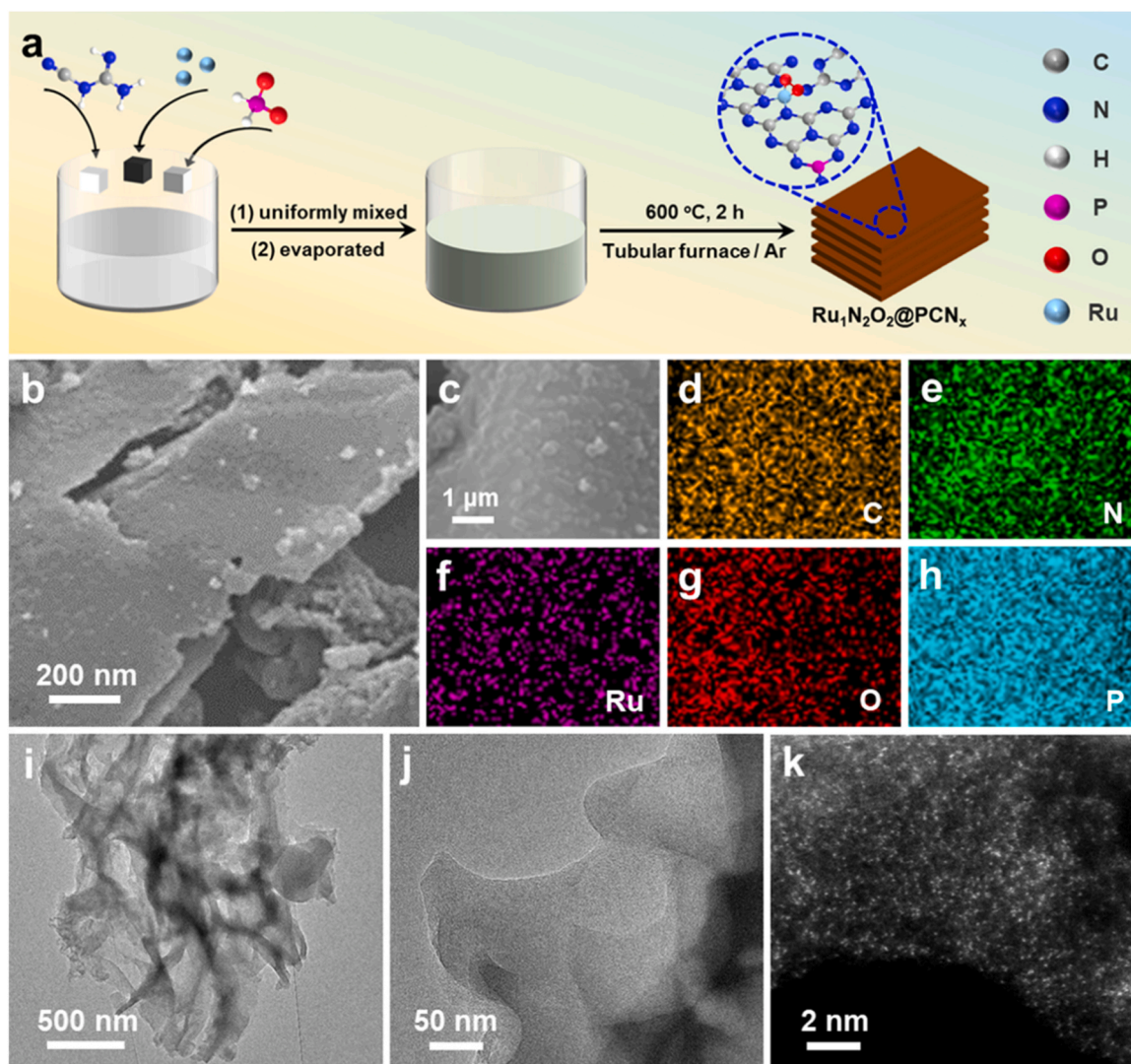
Fig. 1. Schematic illustration for the synthesis of $Ru_1N_2O_2@PCN_x$ (a). SEM (b, c) and elemental mapping images of $Ru_1N_2O_2@PCN_{1.0}$: C (d), N (e), Ru (f), O (g), and P (h). TEM (i, j) and HAADF-STEM (k) images of $Ru_1N_2O_2@PCN_{1.0}$.

plasma optical emission spectrometer (ICP-OES).

3.2. Structure analysis of photocatalysts

Fig. 2a and b show X-ray diffraction (XRD) patterns. CN exhibited two strong diffraction peaks at 12.9° and 27.7°, corresponding to the (100) and (002) crystal planes of CN. For PCN, $Ru_1N_2O_2@CN_{1.0}$ and $Ru_1N_2O_2@PCN_x$, such two peaks were weakened and broadened. This may be attributed to the reaction between metal ions and CN during thermal polymerization, leading to the destruction of the ordered CN framework and the formation of cyano groups [30,31]. However, no prominent diffraction peaks associated with Ru-based compounds were observed in $Ru_1N_2O_2@PCN_x$, suggesting that Ru elements were doped into the matrix, which agreed with the AC HAADF-STEM results (Fig. 1k). From Fourier transform infrared (FT-IR) results (Fig. 2c,d), all samples contained characteristic peaks located at 3000–3500 cm^{-1} for the stretching vibration of N-H. A series of diffraction peaks at 1200–1700 cm^{-1} were induced by the stretching vibrations of aromatic C-N heterocycles. The peak at 810 cm^{-1} corresponded to the bending vibration mode of the heptazine unit [30]. For PCN, $Ru_1N_2O_2@CN_{1.0}$ and $Ru_1N_2O_2@PCN_x$, a new diffraction peak located at 2179 cm^{-1} was assigned to the -C≡N, which originated from the broken of the N-C≡N hybridization in the melon polymerization matrix [31]. The presence of

the -C≡N in PCN, $Ru_1N_2O_2@CN_{1.0}$ and $Ru_1N_2O_2@PCN_x$ can serve as an electron acceptor to promote charge transfer [32,33].

X-ray photoelectron spectroscopy (XPS) was performed to analyze the $Ru_1N_2O_2@PCN_{1.0}$. XPS survey spectrum of $Ru_1N_2O_2@PCN_{1.0}$ confirmed the presence of C, N, O, P, and Ru. (Fig. S3). As shown in Fig. 2e, the high-resolution C 1s spectrum of $Ru_1N_2O_2@PCN_{1.0}$ predominantly contained three carbon configurations, locating at 288.2 (N=C-N), 286.6 (-C≡N), and 284.8 eV (C-C), respectively, in line with the FT-IR analysis [34]. In addition, two peaks centered at 285.6 and 281.2 eV were ascribed to Ru $3d_{3/2}$ and Ru $3d_{5/2}$, respectively, demonstrating the different oxidation states of $Ru^{\delta+}$ $(0 < \delta < 4)$ in $Ru_1N_2O_2@PCN_{1.0}$ [16,35]. The interaction between atomically dispersed Ru species with the carrier was further revealed by Ru 3p XPS spectrum (Fig. 2f) due to the partial overlap of C 1s and Ru 3d spectra, revealing the coexistence of Ru^{4+} (464.4 eV, 76.9%) and Ru^0 (462.2 eV, 23.1%) in $Ru_1N_2O_2@PCN_{1.0}$ [36,37]. For the N 1s spectrum of $Ru_1N_2O_2@PCN_{1.0}$ (Fig. 2g), three typical peaks for $-NH_x$ (amino N), $N-(C)_3$ (pyrrole nitrogen), and C-N=C (pyridine nitrogen) were observed at 401.1 eV, 399.3 eV and 398.2 eV, respectively [30]. More importantly, a Ru-N-associated binding energy peak located at 398.9 eV was observed from the N 1s spectrum, further confirming the presence of Ru single atoms [35]. The O 1s XPS spectrum (Fig. 2h) for $Ru_1N_2O_2@PCN_{1.0}$ displayed four peaks at 534.2, 532.1, 531.2, and 529.6 eV,
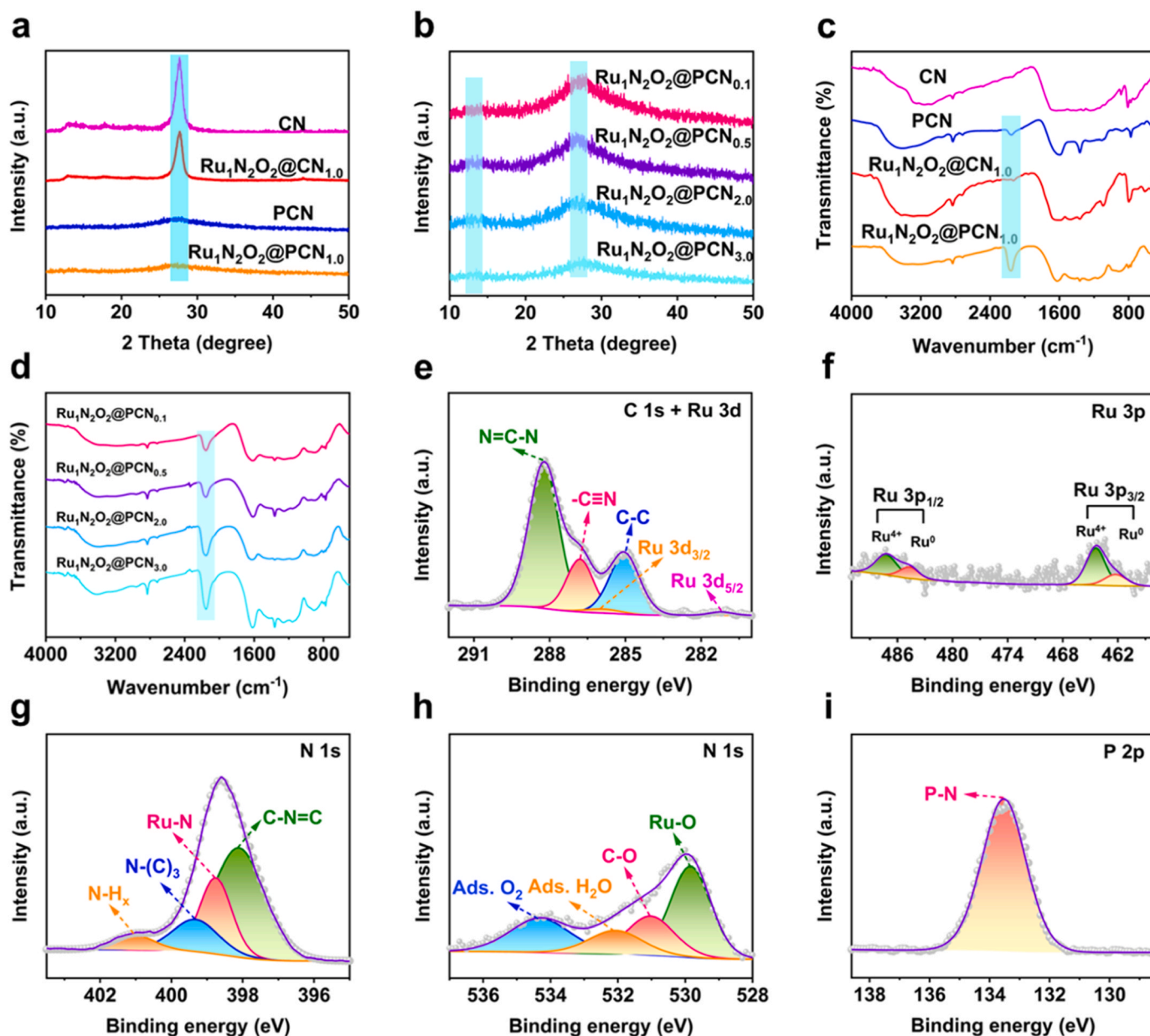
Fig. 2. (a) XRD patterns of CN, $Ru_1N_2O_2@CN_{1.0}$, PCN, and $Ru_1N_2O_2@PCN_{1.0}$. (b) XRD patterns of $Ru_1N_2O_2@PCN_{0.1}$, $Ru_1N_2O_2@PCN_{0.5}$, $Ru_1N_2O_2@PCN_{2.0}$, and $Ru_1N_2O_2@PCN_{3.0}$. (c) FT-IR spectra of CN, PCN, $Ru_1N_2O_2@CN_{1.0}$, and $Ru_1N_2O_2@PCN_{1.0}$. (d) FT-IR spectra of $Ru_1N_2O_2@PCN_{0.1}$, $Ru_1N_2O_2@PCN_{0.5}$, $Ru_1N_2O_2@PCN_{2.0}$, and $Ru_1N_2O_2@PCN_{3.0}$. XPS high-resolution spectra of $Ru_1N_2O_2@PCN_{1.0}$: C 1s+Ru 3d (e), Ru 3p (f), N 1s (g), O 1s (h), and P 2p (i).

corresponding to the absorbed oxygen, absorbed water, C-O bond, and Ru-O bond, respectively [38,39]. The P 2p high-resolution spectrum (Fig. 2i) contained only one peak at 133.5 eV, which was ascribed to the P-N bond, implying that P substituted C in the framework of CN [26].

To further examine the chemical state and coordination environment of Ru single atoms, X-ray absorption near-edge structure (XANES) and extended X-ray absorption fine structure (EXAFS) spectroscopy analysis of $Ru_1N_2O_2@PCN_{1.0}$ were performed. For the Ru K-edge spectrum (Fig. 3a), the absorption edge of $Ru_1N_2O_2@PCN_{1.0}$ between the Ru foil and RuO_2 confirmed the Ru species is in the positive valence state. As shown in Fig. 3b, the Fourier-transformed k^3-weighted EXAFS spectrum of $Ru_1N_2O_2@PCN_{1.0}$ revealed the main peak at 1.47 Å, corresponding to the Ru-N/O coordination shell, indicating that Ru single atoms were doped into CN, according to the AC-HAADF-STEM results. Furthermore, from the wavelet transform (WT) contour map of $Ru_1N_2O_2@PCN_{1.0}$ (Fig. 3c), only one intensity optimum was detected at 4.3 $Å^{-1}$, which was ascribed to Ru-N(O) coordination in the absence of Ru-Ru signal. To

extract the chemical configuration, the quantitative EXAFS fitting of $Ru_1N_2O_2@PCN_{1.0}$ was performed (Fig. 3d, e and Table S1), in which the coordination numbers and bond distance of Ru-N/O were 4.2 ± 0.2 and 2.01 Å, respectively. It was reported that the presence of adjacent atoms (e.g., C, N, or O) in the coordination shells of $Ru_1N_2O_2@PCN_{1.0}$ could not be distinguished by this characterization, which was attributed to the fact that EXAFS scattering was proportional to the number of electrons in the adjacent atoms [16,40]. Besides, according to quantitative EXAFS fitting analysis (Table S2), Ru-P coordination was absent in $Ru_1N_2O_2@PCN_{1.0}$ and the P atom was present in the form of P-N bonds.

To further elucidate the coordination form of Ru atoms in $Ru_1N_2O_2@PCN_{1.0}$, a series of possible Ru coordination models (Fig. S4a-g) were constructed in the heptazine ring structure of CN and DFT calculations were performed. DFT calculation results show that the Ru atom is difficult to form a four-coordinated structure (e.g., Ru-N_1O_3, and Ru-N_3O_1 coordination, etc.) with the N or O atoms of the CN matrix. The calculated XANES spectra of the different optimized structures (Fig. S4e-
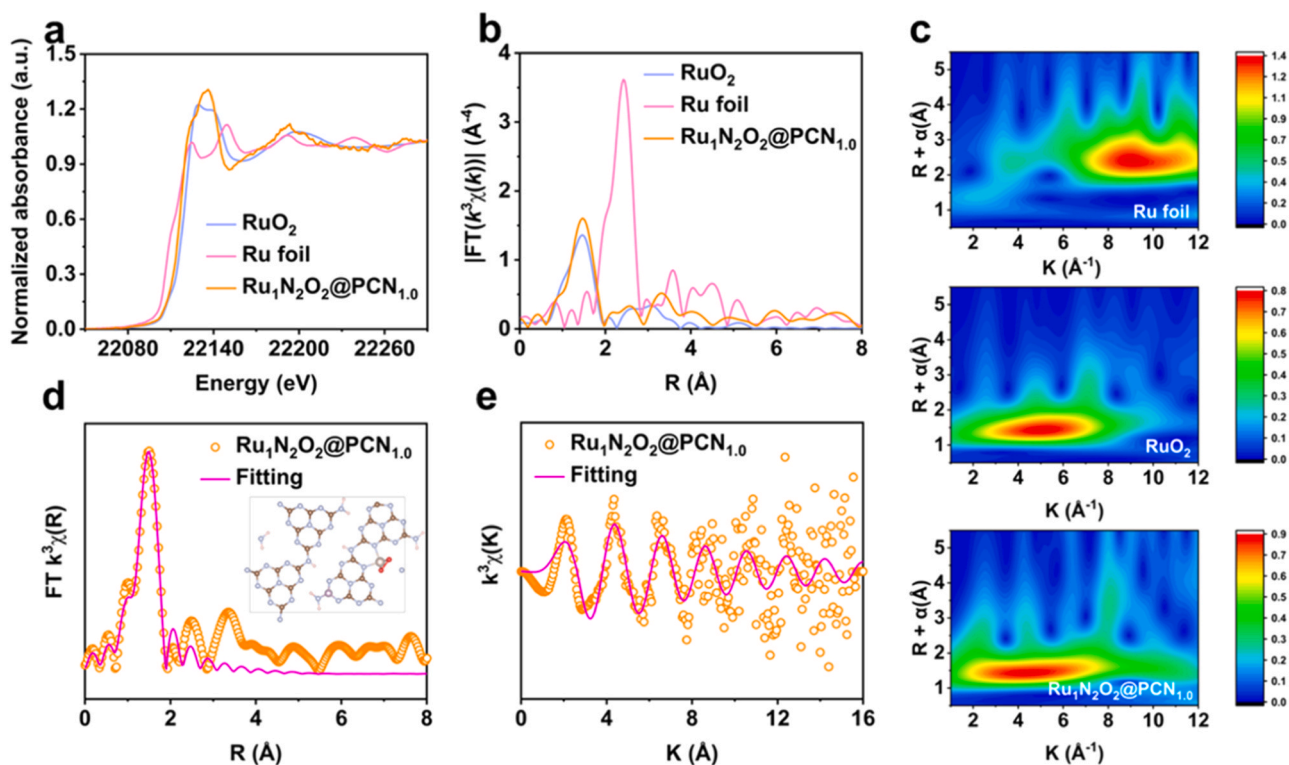
Fig. 3. (a) Normalized Ru K-edge XANES spectra of RuO_2, Ru foil and $Ru_1N_2O_2@PCN_{1.0}$. (b) Fourier transform (FT) at the Ru K-edge of RuO_2, Ru foil and $Ru_1N_2O_2@PCN_{1.0}$. (c) Wavelet transform (WT) of RuO_2, Ru foil and $Ru_1N_2O_2@PCN_{1.0}$. (d) EXAFS fitting spectra in R-space of $Ru_1N_2O_2@PCN_{1.0}$. The inset shows the structure of the P and Ru sites in $Ru_1N_2O_2@PCN_{1.0}$. (e) EXAFS fitting spectra in k-space of $Ru_1N_2O_2@PCN_{1.0}$.

g) show that the Ru-N_2 coordination anchored within the oxygen-free doped cavity agrees better with the experimental spectrum. Thus, the quantitative EXAFS fitting analysis coupled with DFT calculations indicate that the Ru atom is present in $Ru_1N_2O_2@PCN_{1.0}$ in the form of Ru-N_2O_2 coordination. Fig. S4h shows the optimal $Ru_1N_2O_2@PCN_{1.0}$ optimized structure with Ru-N_2O_2 coordination. To clarify the P sites and Ru-N_2O_2 coordination in CN, DFT calculations were employed.

Possible substitution models were constructed. Fig. 4a-e show the fully relaxed atomic structures. When the Ru-N_2O_2 coordination position was determined, the calculated formation energies (E_{form}) indicate that C3 site ($E_{form} = -0.11$ eV) was more stable than other C sites for P-substitution (Fig. 4f). Hence, the optimal structural model of $Ru_1N_2O_2@PCN_{1.0}$ containing Ru-N_2O_2 coordination and P-N bonds was obtained, as shown in the inset of Fig. 3d.
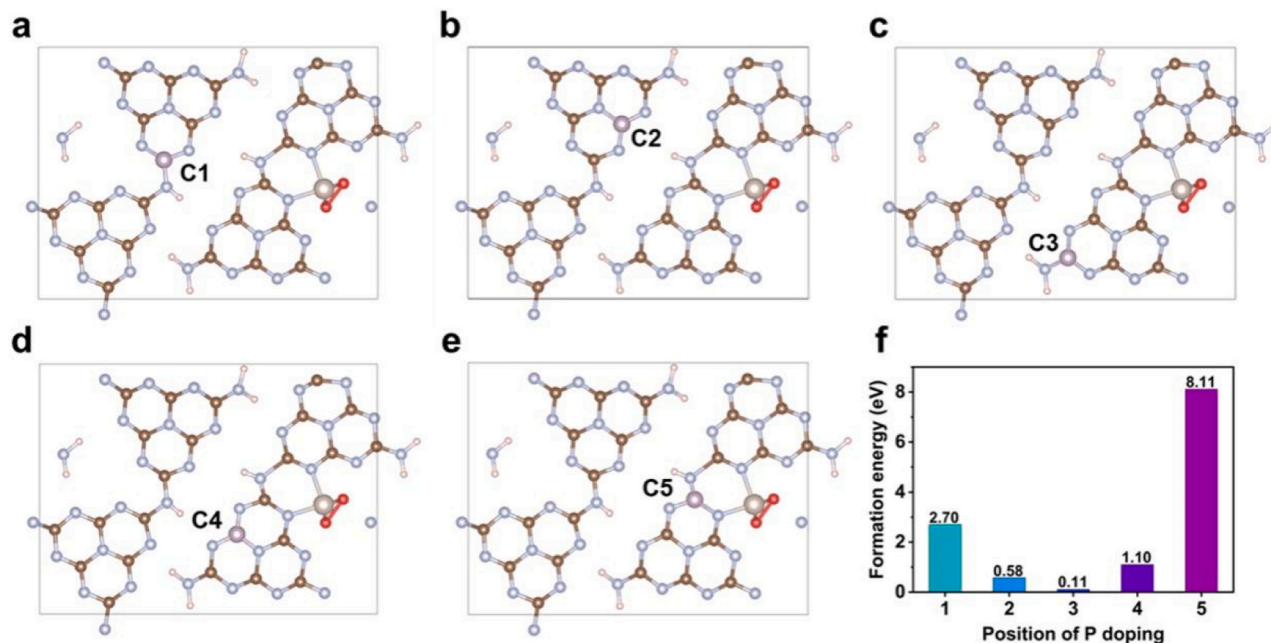

Fig. 4. Top views of the fully relaxed structures of $Ru_1N_2O_2@PCN_{1.0}$ with P substituted at different C sites (a-e). Formation energies of P substitution at different C sites in $Ru_1N_2O_2@PCN_{1.0}$ (f). Brown, gray, red, light brown, and lavender colors represent carbon, nitrogen, oxygen, ruthenium, and phosphorus, respectively.

3.3. Optical and electrical properties

The optical properties of CN, PCN, $Ru_1N_2O_2@CN_{1.0}$, and $Ru_1N_2O_2@PCN_{1.0}$ were determined by UV–vis diffuse reflectance spectroscopy (DRS). As shown in Figs. 5a and S5, the visible light-harvesting capacities of PCN, $Ru_1N_2O_2@CN_{1.0}$ and $Ru_1N_2O_2@PCN_{1.0}$ were significantly enhanced as compared with CN. The Mott-Schottky plots were employed to analyze the flat-band potential (E_{FB}) of all samples. The positive slope Mott-Schottky curves of CN, PCN, $Ru_1N_2O_2@CN_{1.0}$, and $Ru_1N_2O_2@PCN_{1.0}$ (Figs. 5b, c and S6) suggested the n-type nature. As previous report [41], the E_{FB} of an n-type semiconductor is 0.2 V more than its conduction band potential (E_{CB}). In addition, the E_{CB} for CN, PCN, $Ru_1N_2O_2@CN_{1.0}$, and $Ru_1N_2O_2@PCN_{1.0}$ are −1.38, −1.11, 0.92, and −1.06 V vs. Ag/AgCl electrodes, respectively. Meanwhile, the Ag/AgCl electrode of E_{CB} should be calculated as a normal hydrogen electrode (NHE.) using the Nernst equation ($E_{NHE.} = E_{Ag/AgCl} + 0.197$, pH = 7). Hence, the E_{CB} is approximately equal to the E_{FB}, and the E_{CB} of CN, PCN, $Ru_1N_2O_2@CN_{1.0}$, and $Ru_1N_2O_2@PCN_{1.0}$ are −1.18, −0.91, −0.72, and −0.86 V vs. NHE., respectively. Furthermore, the valence band XPS spectra (Figs. 5d and S7) demonstrate the valance band potentials (E_{VB}) of CN, PCN, $Ru_1N_2O_2@CN_{1.0}$, and $Ru_1N_2O_2@PCN_{1.0}$ are 1.71, 1.87, 1.87, and 1.89 eV, respectively [29,42]. A more positive valence band potential of $Ru_1N_2O_2@PCN_{1.0}$ indicates a higher oxidation capacity. Then, according to the formation that $E_g = E_{VB} - E_{CB}$, the bandgaps (E_g) of CN, PCN, $Ru_1N_2O_2@CN_{1.0}$, and $Ru_1N_2O_2@PCN_{1.0}$ are obtained as 2.89, 2.78, 2.59, and 2.75 eV, respectively. The schematic energy band structures of all samples are given in Fig. S8. Furthermore, the calculated band structures and density of states (DOSs) of CN, PCN,

$Ru_1N_2O_2@CN_{1.0}$, and $Ru_1N_2O_2@PCN_{1.0}$ are calculated. As shown in Fig. 5e-l, the variation trend of E_g upon the introduction of Ru and P is consistent with experimental results, although DFT calculations frequently underestimate the E_g of semiconductors compared with experimental measurement. DOSs analysis indicates that the VB edges are predominantly influenced by Ru 3d orbital in $Ru_1N_2O_2@PCN_{1.0}$, while the CB edges are contributed by Ru 3d, C 2p and N 2p orbitals.

The photoinduced charge separation efficiencies of CN, PCN, $Ru_1N_2O_2@CN_{1.0}$, and $Ru_1N_2O_2@PCN_{1.0}$ were further evaluated by steady-state photoluminescence (PL) emission spectroscopy. As shown in Fig. 6a, the PL intensities of the P-doped samples are much lower than those of CN and $Ru_1N_2O_2@CN_{1.0}$, especially for $Ru_1N_2O_2@PCN_{1.0}$, indicating that the P doping into CN effectively inhibits the recombination of photogenerated carriers. Such an increase in electron transfer caused by P doping into CN was further verified by the higher photocurrent density from photocurrent response spectra (Fig. 6b) and the smaller Nyquist arc radius in electrochemical impedance spectra (EIS) (Fig. 6c). More importantly, the transient open-circuit voltage decay (OCVD) results in Fig. S9 show that the photovoltage of $Ru_1N_2O_2@PCN_{1.0}$ is higher than that of CN, suggesting the presence of charge carriers with higher energy. Meanwhile, the photovoltage of $Ru_1N_2O_2@PCN_{1.0}$ decays more slowly as compared with CN, demonstrating the longer lifetime of the charge carriers in $Ru_1N_2O_2@PCN_{1.0}$ [43]. The highest occupied molecular orbital (HOMO) and lowest unoccupied molecular orbital (LUMO) of CN, PCN, $Ru_1N_2O_2@CN_{1.0}$, and $Ru_1N_2O_2@PCN_{1.0}$ (Fig. 6d-g) illustrate that the charge distribution has also been changed after the introduction of the P and Ru dual sites. The spatial distributions of the HOMO and LUMO of CN, PCN and

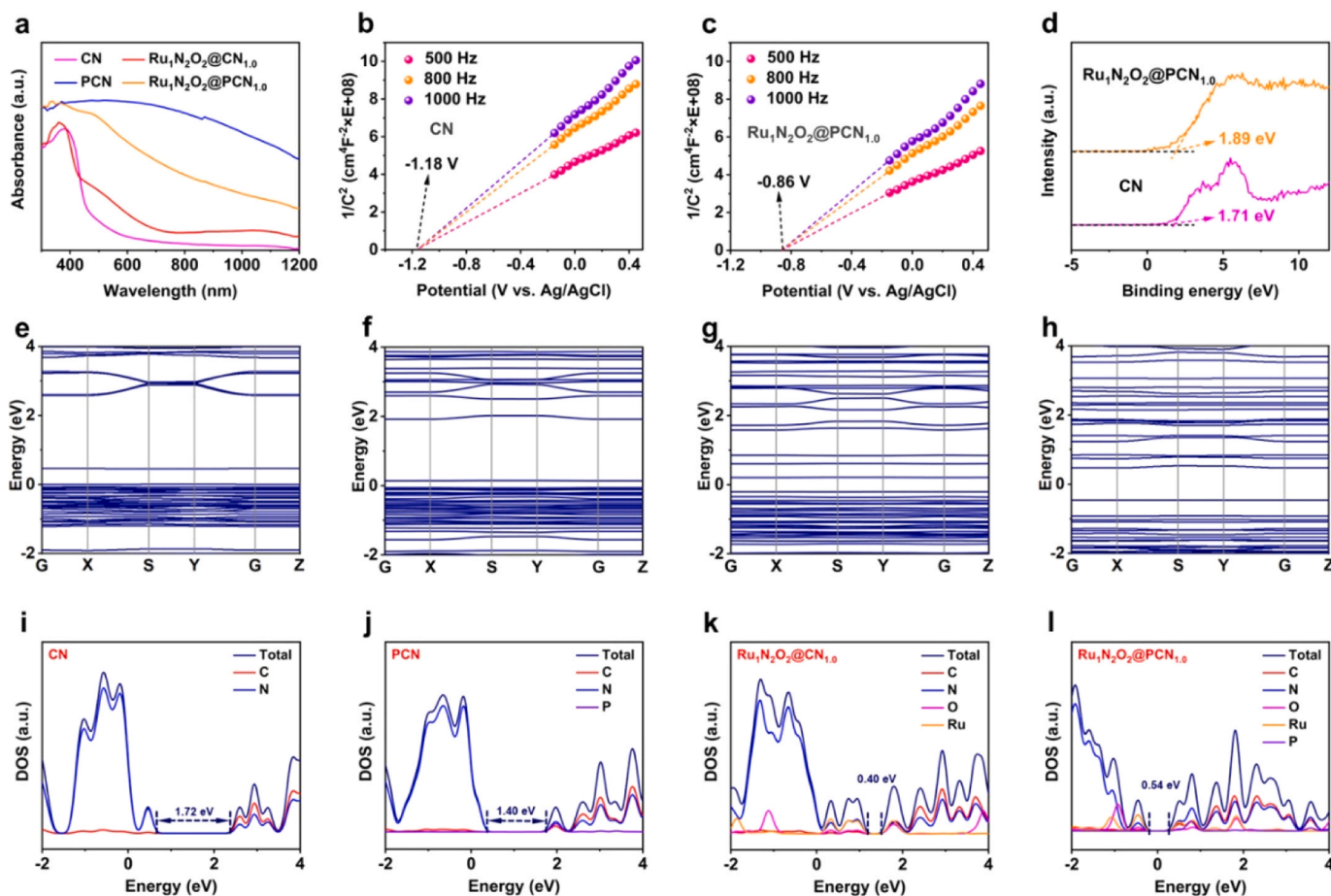**Fig. 5.** (a) UV–vis diffuse reflection spectra of the as-synthesized catalysts. Mott-Schottky plots of CN (b) and $Ru_1N_2O_2@PCN_{1.0}$ (c). VB XPS spectra of CN and $Ru_1N_2O_2@PCN_{1.0}$ (d). Electronic band structures of CN (e), PCN (f), $Ru_1N_2O_2@CN_{1.0}$ (g), and $Ru_1N_2O_2@PCN_{1.0}$ (h). Calculated DOSs of CN (i), PCN (j), $Ru_1N_2O_2@CN_{1.0}$ (k), and $Ru_1N_2O_2@PCN_{1.0}$ (l).
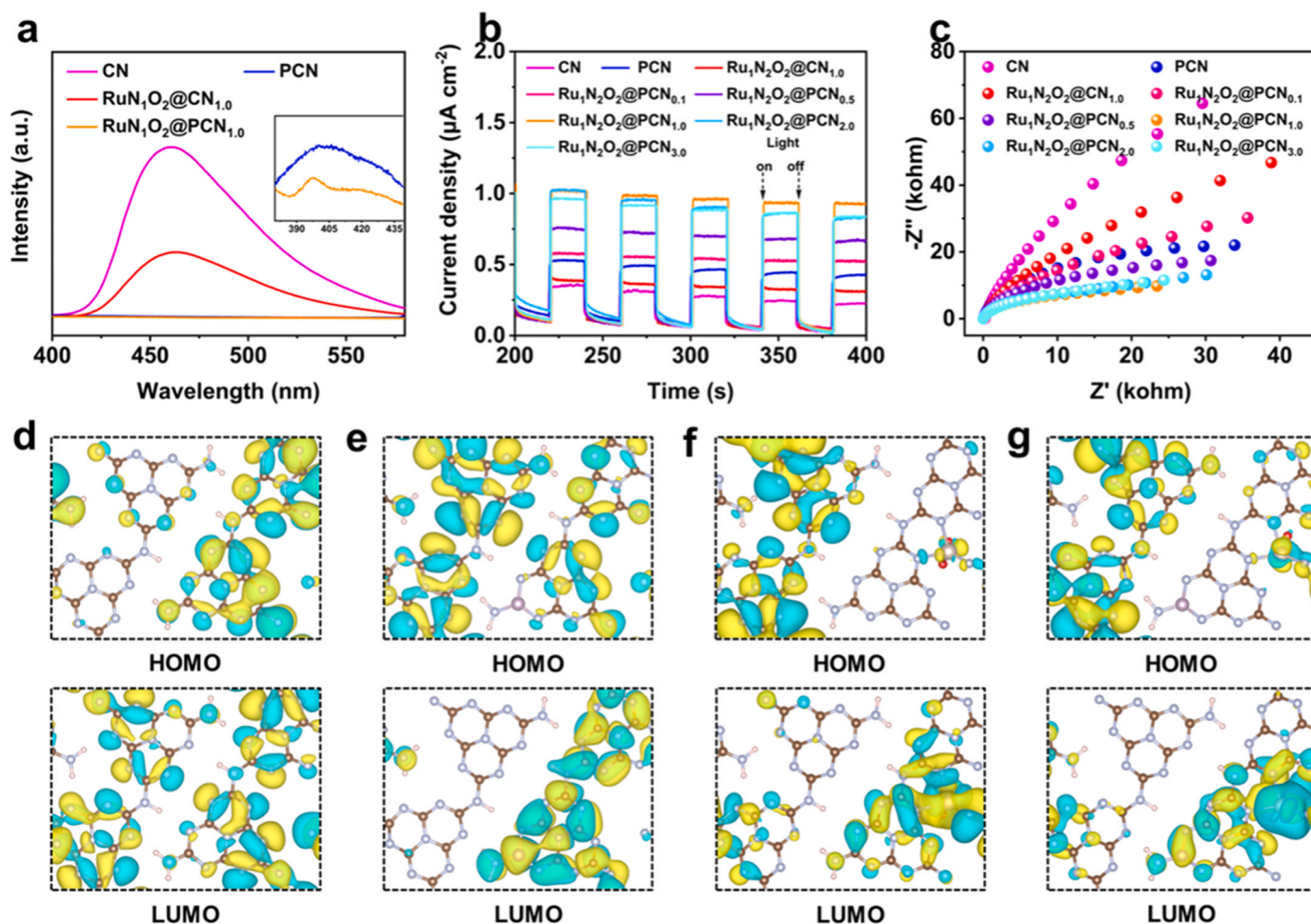
Fig. 6. Steady-state photoluminescence (PL) emission curves (a), transient photocurrent curves (b), and electrochemical impedance spectra (c) of the as-synthesized catalysts. HOMO and LUMO distributions of CN (d), PCN (e), $Ru_1N_2O_2@CN_{1.0}$ (f), and $Ru_1N_2O_2@PCN_{1.0}$ (g). Brown, gray, red, light brown, and lavender colors represent carbon, nitrogen, oxygen, ruthenium, and phosphorus, respectively; the cyan and yellow areas represent electron depletion and accumulation, respectively.

$Ru_1N_2O_2@CN_{1.0}$ were partially overlapped. By comparison, the heavier delocalization of HOMO and LUMO in $Ru_1N_2O_2@PCN_{1.0}$, especially on the doped P site, indicates spatial separations of charge carriers. These results suggested that the dual sites of Ru and P atoms played essential roles in improving the visible light absorption and charge migration/separation ability of $Ru_1N_2O_2@PCN_x$.

3.4. The evaluation of photocatalytic performance

The photocatalytic performances of $Ru_1N_2O_2@PCN_{1.0}$ in biomass refining coupling with CO_2 reduction were firstly investigated in the solution of 1.0 M KOH containing xylose under irradiation by a 10 W Vlight lamp. The primary liquid and gas products detected in the reaction system were lactic acid (72.7%) and CO (801.1 μmol g^{-1}), respectively (Table 1, entry 1). A series of experiments were performed to identify the source of the products. Firstly, only trace amounts of CO and lactic acid were detected when the KOH solution was replaced with a HCl solution or H_2O (Table 1, entries 2,3). Thereafter, the reaction performed in the dark showed a CO production rate of 16.60 μmol g^{-1} and a lactic acid yield of 23.8% (Table 1, entry 4). These results revealed that both the alkaline solution system and light source were essential for this redox reaction. More importantly, in the reaction without CO_2, a certain amount of CO (362.5 μmol g^{-1}) was detected, while the lactic acid yield was as high as 87.7% (Table 1, entry 5). Among them, the lactic acid yield was higher in the Ar atmosphere than in the CO_2 atmosphere, mainly due to the reaction of CO_2 with the hydroxide ions in

Table 1

Comparative study of photocatalytic lactic acid synthesis and CO_2 reduction in different reaction systems (reaction conditions: $Ru_1N_2O_2@PCN_{1.0}$ (10 mg), xylose (150 mg), 8 h, 30 °C, 10 W VLight).

No.	Condition	CO production (μmol g^{-1})	Lactic acid yield (%)
1	CO_2 + Light + KOH (1.0 M)	801.1	72.7
2	CO_2 + Light + H_2O	Trace	Trace
3	CO_2 + Light + HCl (1.0 M)	Trace	Trace
4	CO_2 + Dark + KOH (1.0 M)	16.6	23.8
5[a]	Light + KOH (1.0 M)	362.5	87.7

[a] Entry 5: Reaction mixture degassed by purging with Ar gas for an extended time period till 15 min to remove completely dissolved gases.

the system to reduce the alkalinity of the reaction system. According to the previous report [44], high alkali concentrations increase the generation of lactic acid, while low alkali concentrations facilitate the production of xylonic acid. Furthermore, the results of the $^{13}CO_2$ isotope experiment (Fig. 7a and S10) revealed that ^{13}CO ($m/z = 29$) was the predominant product, indicating that the carbon atoms of the reduction products were mainly derived from CO_2. In addition, the photocatalytic CO_2 reduction and biomass refining performance of CN, $Ru_1N_2O_2@CN_{1.0}$, PCN, and $Ru_1N_2O_2@PCN_x$ photocatalysts were studied. As
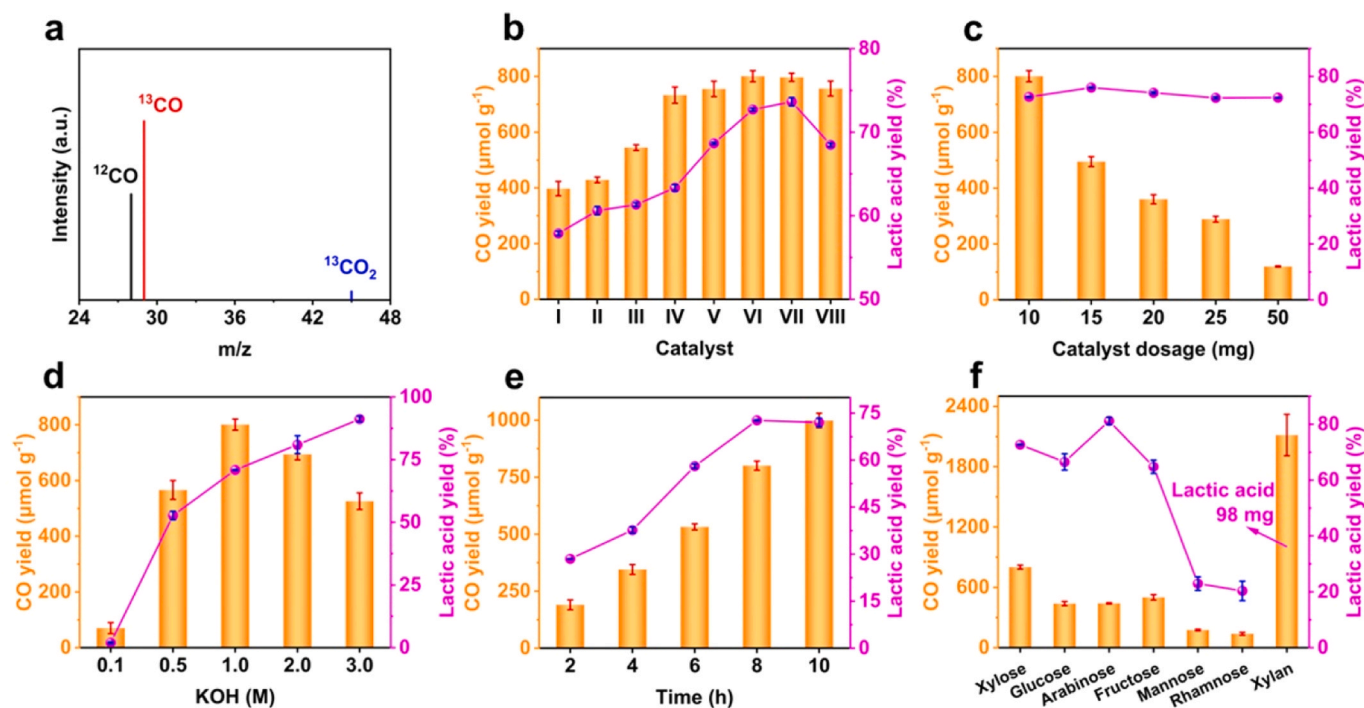
Fig. 7. (a) MS spectrum of the CO generated from the $^{13}CO_2$ isotope experiments. (b) The effects of different photocatalysts on its performance (I: CN, II: $Ru_1N_2O_2@CN_{1.0}$, III: PCN, IV: $Ru_1N_2O_2@PCN_{0.1}$, V: $Ru_1N_2O_2@CN_{0.5}$, VI: $Ru_1N_2O_2@PCN_{1.0}$, VII: $Ru_1N_2O_2@PCN_{2.0}$, VIII: $Ru_1N_2O_2@CN_{3.0}$). The effects of catalyst dosage (c), KOH concentration (d), and reaction time (e) on the performance of $Ru_1N_2O_2@PCN_{1.0}$. (f) Universality tests of $Ru_1N_2O_2@PCN_{1.0}$.

depicted in Fig. 7b, enhanced photocatalytic activity was observed in all modified samples, particularly significant in $Ru_1N_2O_2@PCN_{1.0}$. The performance results for all modified catalysts were consistent with the results of EIS and transient photocurrent spectra. As shown in Fig. S11a, formic acid and glyceraldehyde were detected as the main by-products.

The effects of different conditions (e.g., catalyst dosage, alkali concentration, reaction time) on $Ru_1N_2O_2@PCN_{1.0}$ for simultaneous photocatalytic biomass conversion and CO_2 reduction were studied. As depicted in Fig. 7c, the yields of CO decreased along with the increase of $Ru_1N_2O_2@PCN_{1.0}$ dosage, while the yield of lactic acid rose before it decreased. This result is attributed to the utilization of incident light which may be disturbed by the excess catalyst [41,45]. The optimum yields of CO and lactic acid were 801.1 µmol g^{-1} and 76.0%, respectively. The trend of xylose conversion was opposite to that of CO (Fig. S11b). As shown in Fig. 7d, the properties of CO_2 reduction and xylose conversion were studied at different KOH concentrations. With a higher alkali concentration, the lactic acid yield linearly increased. The elevated hydroxide ion content of the system may facilitate the production of oxidation active species, thus promoting xylose conversion [45]. At the concentration of 3.0 M KOH, the yield of lactic acid reached 91.2%, and the trend of xylose conversion corresponds to lactic acid yield (Fig. S11c). Moreover, better CO generation efficiencies were detected at higher alkali concentrations (1.0 M). Dissolved CO_2 level increases at higher alkali concentrations. A higher concentration of CO_2 near the $Ru_1N_2O_2@PCN_{1.0}$ surface increases the yield of CO. However, the adsorbed $*CO_2$ obtained fewer surface adsorbed protons at an alkali concentration greater than 1.0 M, which hindered further CO_2 reduction [46]. An important factor affecting the simultaneous photocatalytic biomass conversion and CO_2 reduction is the irradiation time. With the extension of irradiation from 2 h to 10 h, the production of CO constantly increased, while the generation of lactic acid decreased after 8 h (Fig. 7e). The explanation for this trend may be that xylose was almost converted (Fig. S11d), leading to further degradation of the generated lactic acid [47]. Furthermore, the previously reported CN-based materials used in CO_2 reduction were summarized in Table S3 [48–54]. The $Ru_1N_2O_2@PCN_{1.0}$ shows enhanced photocatalytic activity

in CO_2 reduction as compared with other CN-based photocatalysts.

The synchronous photocatalytic biorefineries and CO_2 reduction in different biomass systems were conducted using $Ru_1N_2O_2@PCN_{1.0}$. As shown in Fig. 7f, the lactic acid yield and CO evolution of the systems with xylose, glucose, arabinose, fructose, mannose and rhamnose as substrates were 72.7%/801.1 µmol g^{-1}, 66.5%/439.2 µmol g^{-1}, 81.2%/441.1 µmol g^{-1}, 64.8%/501.0 µmol g^{-1}, 23.0%/175.6 µmol g^{-1}, and 20.4%/138.3 µmol g^{-1}, respectively. Furthermore, up to 98 mg of lactic acid and 2114.8 µmol g^{-1} of CO production were also detected within the xylan system. The recycling stability of $Ru_1N_2O_2@PCN_{1.0}$ is essential in synchronous photocatalytic CO_2 reduction and biomass conversion. No significant change was detected in the production of CO and xylose conversion after 5 cycles (40 h) (Fig. 8a). The lactic acid yield decreased from 72.7% to 68.9%, still maintaining 94.8% of its first use. Furthermore, no obvious change of fresh and recycled photocatalysts was observed from the XRD patterns, FT-IR spectra and HAADF-STEM image (Figs. 8b, c and S12). Thus, $Ru_1N_2O_2@PCN_{1.0}$ has excellent universality and recycling stability in the coupling of photocatalytic biorefineries with CO_2 reduction.

3.5. Photocatalytic mechanism and DFT calculations

In-situ high-resolution X-ray photoelectron spectroscopy (XPS) was conducted to speculate on the changes in surface electronic chemical states and active sites of $Ru_1N_2O_2@PCN_{1.0}$ photocatalyst. As shown in Fig. 9a, a positive shift of P 2p could be observed after light irradiation upon $Ru_1N_2O_2@PCN_{1.0}$, which indicated the increases in the valance of P after light irradiation. This result demonstrated the hole capture roles of P atoms in $Ru_1N_2O_2@PCN_{1.0}$ during photocatalytic process. The P single atoms could trap the photogenerated holes, which was beneficial for the accumulation of photogenerated electrons on Ru sites to achieve multi-electron transfer process of CO_2 reduction reaction [27,55,56]. Meanwhile, a negative shift of Ru $3d_{5/2}$ binding energy occurred after light irradiation, which suggested the electron capture roles of Ru atoms in $Ru_1N_2O_2@PCN_{1.0}$ photocatalyst (Fig. 9b).

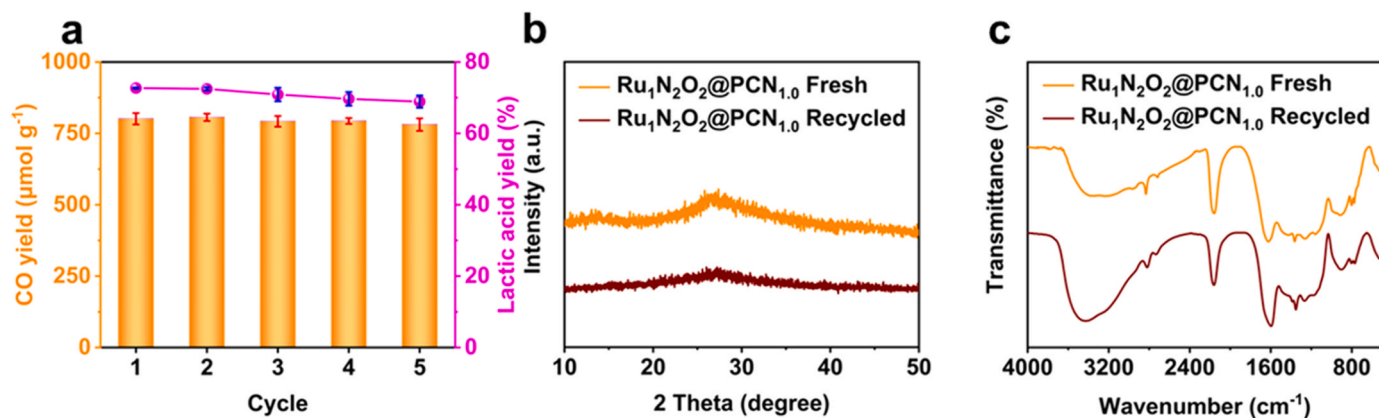Besides, electron spin-resonance (ESR) spectroscopy was used to

Fig. 8. (a) Recycling tests of $Ru_1N_2O_2@PCN_{1.0}$. XRD patterns (b) and FT-IR spectra (c) of $Ru_1N_2O_2@PCN_{1.0}$-fresh and $Ru_1N_2O_2@PCN_{1.0}$-recycled.

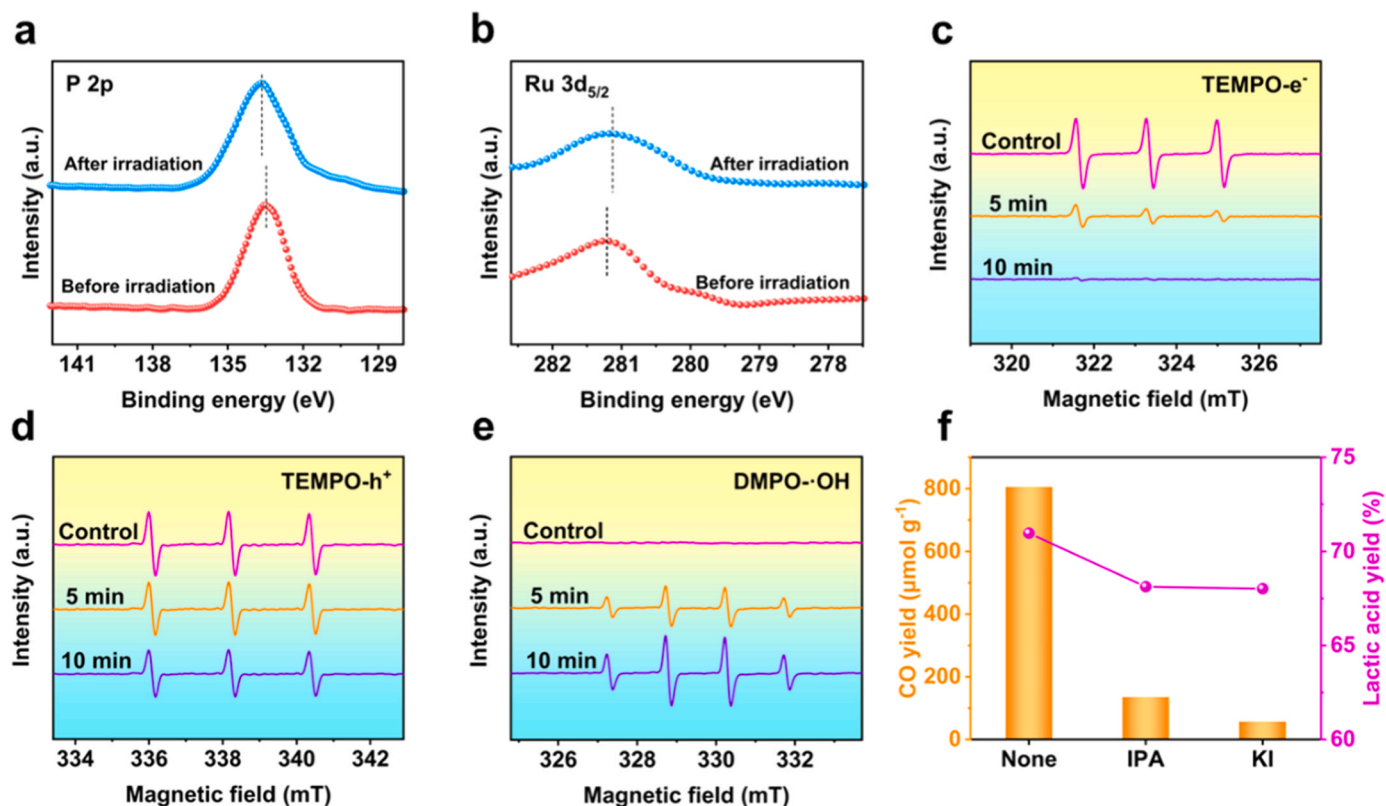**Fig. 9.** The in-situ high-resolution XPS spectra of P 2p (a) and Ru $3d_{5/2}$ (b) over $Ru_1N_2O_2@PCN_{1.0}$ before and after light irradiation. TEMPO ESR spin-labeling for e⁻ (c) and h⁺ (d) of $Ru_1N_2O_2@PCN_{1.0}$. DMPO ESR spin-labeling for·OH (e) of $Ru_1N_2O_2@PCN_{1.0}$. (f) The effects of different oxidation active species on biorefinery and CO_2 reduction photocatalyzed by $Ru_1N_2O_2@PCN_{1.0}$.

detect the presence of electrons (e⁻) and oxidation active species in the $Ru_1N_2O_2@PCN_{1.0}$ system. Initially, 2,2,6,6-tetramethylpiperidine-*N*-oxyl (TEMPO) was used to identify the presence of e⁻ and holes (h⁺). As shown in Fig. 9c, an obvious triple-equal signal peak was detected for the photocatalysts-TEMPO system under dark conditions. The TEMPO signal intensity reduced when the photogenerated e⁻ reacted with TEMPO to form TEMPOH under visible light irradiation. In addition, the TEMPO signal intensity decreases evidently with increasing visible light irradiation time, indicating the generation of more e⁻. The change regularity of h⁺ matches with e⁻, which is a result of the pair production of e⁻ and h⁺ (Fig. 9d) [58]. Furthermore, hydroxyl radicals (·OH) can be spin-trapped by 5,5-dimethyl-1-pyrroline *N*-oxide (DMPO). As shown in Fig. 9e, the signals of DMPO-·OH with an intensity of 1:2:2:1 were presented after 5 min of illumination. Subsequently, the signal intensity

of DMPO-·OH increased with prolonged illumination time, indicating that more·OH was generated [47]. To further explore the impacts of h⁺ and·OH on simultaneous photocatalytic CO_2 reduction and biomass refining, a series of poisoning tests were performed. As depicted in Fig. 9f, when potassium iodide (KI) and isopropyl alcohol (IPA) were added into the reaction systems, respectively, the production of CO was significantly reduced as compared with the system without inhibitors. Meanwhile, the lactic acid yield decreased sequentially. These results indicated that h⁺ and·OH were beneficial to biomass refining and CO_2 reduction.

To further understand the effect of P and Ru dual sites introduction on CO_2 photoreduction, first-principles calculations of the Gibbs free energy (ΔG) for the reduction of CO_2 to CO by PCN, $Ru_1N_2O_2@CN_{1.0}$ and $Ru_1N_2O_2@PCN_{1.0}$ were conducted (Fig. 10a). In general, pathways
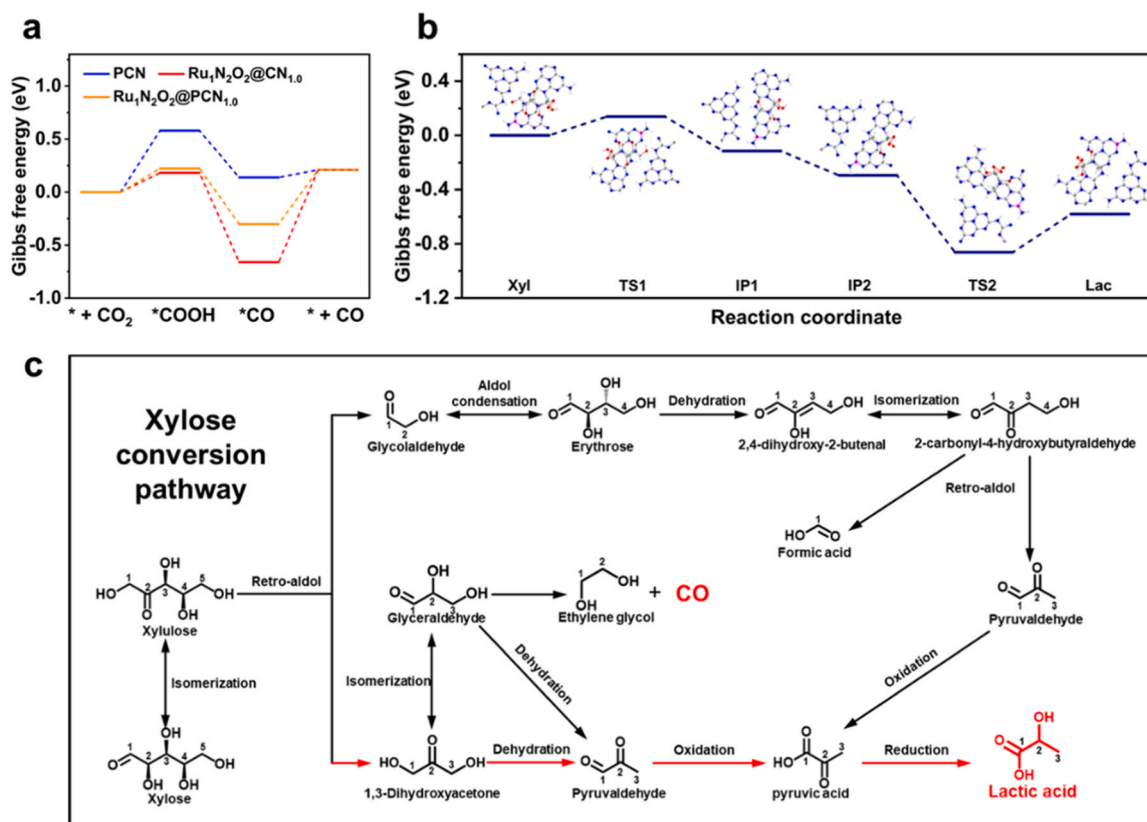
Fig. 10. (a) Calculated Gibbs free energy diagram for photoreduction of CO_2 to CO on PCN, $Ru_1N_2O_2@CN_{1.0}$ and $Ru_1N_2O_2@PCN_{1.0}$. (b) Calculated Gibbs free energy profile for the conversion of xylose into lactic acid on the surface of $Ru_1N_2O_2@PCN_{1.0}$. (c) Possible reaction pathways of xylose photoreforming via $Ru_1N_2O_2@PCN_{1.0}$.

of photocatalytic CO_2 reduction reaction to CO typically proceed in the order of CO_2, $*CO_2$, $*COOH$, $*CO$, and CO, with the potential rate-determining step often attributed to the generation of $*COOH$ ($*CO_2 + H^+ + e^- \rightarrow *COOH$) [26]. The calculated ΔG for the first step of electron-proton transfer ($*CO_2 + H^+ + e^- \rightarrow *COOH$) of PCN was determined to be 0.58 eV. The introduction of $Ru-N_2O_2$ coordination into CN significantly modified the feasibility of this step. For the second step ($*COOH + H^+ + e^- \rightarrow *CO + H_2O$), although $Ru_1N_2O_2@PCN_{1.0}$ exhibited a slight endothermic behavior over $Ru_1N_2O_2@PCN_{1.0}$, the formation of $*CO$ remained thermodynamically favorable, and the desorption barrier for CO from $Ru_1N_2O_2@PCN_{1.0}$ was lower than that of $Ru_1N_2O_2@CN_{1.0}$.

Based on the above-mentioned results and previous reports [10,45, 57–62], the calculated conversion pathway of xylose into lactic acid on the surface of $Ru_1N_2O_2@PCN_{1.0}$ and the geometry of various transition states (TS) and intermediate products (IP) along the reaction channel are presented in Fig. 10b. The first step is the isomerization process of xylose, which required an activation energy of 0.14 eV to form xylulose (TS1). Then, the C3-C4 bond is cleaved in TS1 with an activation energy barrier of −0.12 eV, resulting in the facilitated conversion of TS1 into dihydroxyacetone (IP1) and glycolaldehyde. In the next step, IP1 is dehydrated to form pyruvaldehyde (IP2), which then accepts a hydroxyl group on the terminal C(-CHO) through an endothermic reaction with a reaction barrier of −0.86 eV to form pyruvic acid (TS2). Following further rearrangement and hydration of TS2, a final stable lactic acid product is finally formed with a total reaction energy of −0.58 eV. Moreover, we propose a complete mechanism for the conversion of xylose to lactic acid, which includes a potential pathway for the conversion of glycolaldehyde to lactic acid, as shown in Fig. 10c. Initially, xylose is isomerized to xylulose in the presence of OH⁻ and then the C3-C4 bond of xylulose is cleaved to glycolaldehyde and 1,3-dihydroxyacetone via retro-aldol condensation [57]. Subsequently, pyruvaldehyde

is formed through the dehydration of 1,3-dihydroxyacetone or its isomerization product (glyceraldehyde) [58]. Under alkaline conditions, pyruvaldehyde undergoes oxidation to form pyruvic acid, which is subsequently reduced to lactic acid [45]. Another potential pathway for lactic acid synthesis involves multiple intermediates. Specifically, glycolaldehyde is produced as erythrose by an aldol condensation reaction [58]. Then, erythrose is dehydrated and isomerized to form 2-carbonyl-4-hydroxybutyraldehyde, which is further decomposed by retro-aldol condensation to pyruvaldehyde and formic acid [58]. Lactic acid is ultimately produced by the oxidation and reduction of pyruvaldehyde. Furthermore, CO can be derived from the subsequent decomposition of glyceraldehyde [59–61].

4. Conclusions

In summary, we successfully prepared a novel photocatalyst comprising of Ru and P dual sites anchored on CN ($Ru_1N_2O_2@PCN_x$) using a pre-assembled pyrolysis strategy. Benefiting from $Ru-N_2O_2$ and P-N coordination, $Ru_1N_2O_2@PCN_{1.0}$ was proved to possess excellent performance on CO_2 reduction and biomass conversion (CO: 100.1 μmol g^{-1} h^{-1}; lactic acid: 91.2%). Furthermore, the $Ru_1N_2O_2@PCN_{1.0}$ had excellent universality and was successfully used in biomass-derived monosaccharides and xylan systems. Experimental analysis coupled with DFT calculations demonstrated that P-atom doping into CN promoted charge transfer/separation, while the presence of $Ru-N_2O_2$ coordination regulated the electronic structure of CN and reduced the reaction energy barrier. This work not only designs an efficient photocatalyst to achieve synchronous photocatalytic biomass conversion and CO_2 reduction in aqueous media, but also offers new insights into alleviating the greenhouse effect and achieving carbon neutrality.

CRediT authorship contribution statement

Zhendong Liu: Conceptualization, Methodology, Investigation, Data curation, Writing – original draft, Visualization. **Jiliang Ma:** Conceptualization, Investigation, Project administration, Methodology, Supervision, Writing – review & editing, Funding acquisition. **Yanzhu Guo:** Validation, Writing – review & editing. **Min Hong:** DFT calculations, Writing – review & editing. **Runcang Sun:** Resources, Investigation, Project administration, Supervision, Writing – review & editing.

Declaration of Competing Interest

The authors declare that they have no known competing financial interests or personal relationships that could have appeared to influence the work reported in this paper.

Data availability

Data will be made available on request.

Acknowledgments

Appendix A. Supporting information

Supplementary data associated with this article can be found in the online version at doi:10.1016/j.apcatb.2023.123429.

References

[1] D.A. Lashof, D.R. Ahuja, Relative contributions of greenhouse gas emissions to global warming, Nature 344 (1990) 529–531.
[2] Z. Liu, Z. Deng, S. Davis, P. Ciais, Monitoring global carbon emissions in 2022, Nat. Rev. Earth Environ. 4 (2023) 205–206.
[3] A. White, M.G.R. Cannell, A.D. Friend, CO_2 stabilization, climate change and the terrestrial carbon sink, Glob. Change Biol. 6 (2000) 817–833.
[4] M. Chai, S. Razavi Bazaz, R. Daiyan, A. Razmjou, M. Ebrahimi Warkiani, R. Amal, V. Chen, Biocatalytic micromixer coated with enzyme-MOF thin film for CO_2 conversion to formic acid, Chem. Eng. J. 426 (2021), 130856.
[5] I. Hussain, H. Alasiri, W. Ullah Khan, K. Alhooshani, Advanced electrocatalytic technologies for conversion of carbon dioxide into methanol by electrochemical reduction: recent progress and future perspectives, Coord. Chem. Rev. 482 (2023), 215081.
[6] F. Besharat, F. Ahmadpoor, Z. Nezafat, M. Nasrollahzadeh, N.R. Manwar, P. Fornasiero, M.B. Gawande, Advances in carbon nitride-based materials and their electrocatalytic applications, ACS Catal. 12 (2022) 5605–5660.
[7] J. Liang, H. Yu, J. Shi, B. Li, L. Wu, M. Wang, Dislocated bilayer MOF enables high-selectivity photocatalytic reduction of CO_2 to CO, Adv. Mater. 35 (2023) 2209814.
[8] A.V. Puga, Photocatalytic production of hydrogen from biomass-derived feedstocks, Coord. Chem. Rev. 315 (2016) 1–66.
[9] J. Ma, X. Li, Y. Li, G. Jiao, H. Su, D. Xiao, S. Zhai, R. Sun, Single-atom zinc catalyst for co-production of hydrogen and fine chemicals in soluble biomass solution, Adv. Powder Mater. 1 (2022) 100058.
[10] E. Lam, M. Miller, S. Linley, R.R. Manuel, I.A.C. Pereira, E. Reisner, Comproportionation of CO_2 and cellulose to formate using a floating semiconductor-enzyme photoreforming catalyst, Angew. Chem. Int. Ed. 62 (2023), e202215894.
[11] B. Dai, J. Guo, C. Gao, H. Yin, Y. Xie, Z. Lin, Recent advances in efficient photocatalysis via modulation of electric and magnetic fields and reactive phase control, Adv. Mater. 35 (2023) 2210914.
[12] P. Melchiorre, Introduction: photochemical catalytic processes, Chem. Rev. 122 (2022) 1483–1484.
[13] X. Lin, S.-F. Ng, W.-J. Ong, Coordinating single-atom catalysts on two-dimensional nanomaterials: a paradigm towards bolstered photocatalytic energy conversion, Coord. Chem. Rev. 471 (2022) 214743.
[14] J. Xi, H.S. Jung, Y. Xu, F. Xiao, J.W. Bae, S. Wang, Synthesis strategies, catalytic applications, and performance regulation of single-atom catalysts, Adv. Funct. Mater. 31 (2021) 2008318.
[15] X.-H. Jiang, L.-S. Zhang, H.-Y. Liu, D.-S. Wu, F.-Y. Wu, L. Tian, L.-L. Liu, J.-P. Zou, S.-L. Luo, B.-B. Chen, Silver single atom in carbon nitride catalyst for highly efficient photocatalytic hydrogen evolution, Angew. Chem. Int. Ed. 59 (2020) 23112–23116.
[16] P. Sharma, S. Kumar, O. Tomanec, M. Petr, J. Zhu Chen, J.T. Miller, R.S. Varma, M.B. Gawande, R. Zbořil, Carbon nitride-based ruthenium single atom photocatalyst for CO_2 reduction to methanol, Small 17 (2021) 2006478.
[17] Y.-Z. Zhang, C. Liang, H.-P. Feng, W. Liu, Nickel single atoms anchored on ultrathin carbon nitride for selective hydrogen peroxide generation with enhanced photocatalytic activity, Chem. Eng. J. 446 (2022), 137379.
[18] W. Tang, H. Zhang, X. Yang, Z. Dai, Y. Sun, H. Liu, Z. Hu, X. Zheng, Ru single atom catalyst with dual reaction sites for efficient fenton-like degradation of organic contaminants, Appl. Catal. B Environ. 320 (2023), 121952.
[19] Z.-H. Xue, D. Luan, H. Zhang, X.W. Lou, Single-atom catalysts for photocatalytic energy conversion, Joule 6 (2022) 92–133.
[20] Y. Zheng, L. Lin, B. Wang, X. Wang, Graphitic carbon nitride polymers toward sustainable photoredox catalysis, Angew. Chem. Int. Ed. 54 (2015) 12868–12884.
[21] J. Wang, S. Wang, A critical review on graphitic carbon nitride (g-C_3N_4)-based materials: preparation, modification and environmental application, Coord. Chem. Rev. 453 (2022), 214338.
[22] Q. Liu, H. Cheng, T. Chen, T.W.B. Lo, Z. Xiang, F. Wang, Regulating the *OCCHO intermediate pathway towards highly selective photocatalytic CO_2 reduction to CH_3CHO over locally crystallized carbon nitride, Energy Environ. Sci. 15 (2022) 225–233.
[23] P. Chen, B. Lei, Xa Dong, H. Wang, J. Sheng, W. Cui, J. Li, Y. Sun, Z. Wang, F. Dong, Rare-earth single-atom La-N charge-transfer bridge on carbon nitride for highly efficient and selective photocatalytic CO_2 reduction, ACS Nano 14 (2020) 15841–15852.
[24] Y. Hu, Y. Qu, Y. Zhou, Z. Wang, H. Wang, B. Yang, Z. Yu, Y. Wu, Single Pt atom-anchored C_3N_4: a bridging Pt-N bond boosted electron transfer for highly efficient photocatalytic H_2 generation, Chem. Eng. J. 412 (2021), 128749.
[25] W. Li, W. Li, Z. Guo, Y. Song, S. Tang, Y. Ma, X. Xing, Q. Wang, Synthesis of atomically thin g-C_3N_4 nanosheets via supercritical CO_2 doping with single-atom cobalt for photocatalytic hydrogen evolution, ACS Appl. Mater. Interfaces 13 (2021) 52560–52570.
[26] X. Sun, L. Sun, G. Li, Y. Tuo, C. Ye, J. Yang, J. Low, X. Yu, J.H. Bitter, Y. Lei, D. Wang, Y. Li, Phosphorus tailors the d-band center of copper atomic sites for efficient CO_2 photoreduction under visible-light irradiation, Angew. Chem. Int. Ed. 61 (2022), e202207677.
[27] G. Wang, Z. Chen, T. Wang, D. Wang, J. Mao, P and Cu dual sites on graphitic carbon nitride for photocatalytic CO_2 reduction to hydrocarbon fuels with high C_2H_6 evolution, Angew. Chem. Int. Ed. 61 (2022), e202210789.
[28] Q. Fan, J. Su, T. Sun, Z. Bi, H. Wang, S. Zhang, Q. Liu, L. Zhang, G. Hu, Advances of the functionalized carbon nitrides for electrocatalysis, Carbon Energy 4 (2022) 211–236.
[29] D. Sun, Y. Chen, X. Yu, Y. Yin, G. Tian, Engineering high-coordinated cerium single-atom sites on carbon nitride nanosheets for efficient photocatalytic amine oxidation and water splitting into hydrogen, Chem. Eng. J. 462 (2023), 142084.
[30] H. Yu, R. Shi, Y. Zhao, T. Bian, Y. Zhao, C. Zhou, G.I.N. Waterhouse, L.-Z. Wu, C.-H. Tung, T. Zhang, Alkali-assisted synthesis of nitrogen deficient graphitic carbon nitride with tunable band structures for efficient visible-light-driven hydrogen evolution, Adv. Mater. 29 (2017) 1605148.
[31] X. Hu, P. Lu, R. Pan, Y. Li, J. Bai, Y. He, C. Zhang, F. Jia, M. Fu, Metal-ion-assisted construction of cyano group defects in g-C_3N_4 to simultaneously degrade wastewater and produce hydrogen, Chem. Eng. J. 423 (2021) 130278.
[32] K. Li, W. Zhou, X. Li, Q. Li, S.A.C. Carabineiro, S. Zhang, J. Fan, K. Lv, Synergistic effect of cyano defects and $CaCO_3$ in graphitic carbon nitride nanosheets for efficient visible-light-driven photocatalytic NO removal, J. Hazard. Mater. 442 (2023) 130040.
[33] C. Cheng, L. Mao, X. Kang, C.-L. Dong, Y.-C. Huang, S. Shen, J. Shi, L. Guo, A high-cyano groups-content amorphous-crystalline carbon nitride isotype heterojunction photocatalyst for high-quantum-yield H_2 production and enhanced CO_2 reduction, Appl. Catal. B Environ. 331 (2023), 122733.
[34] Z. Teng, Q. Zhang, H. Yang, K. Kato, W. Yang, Y.-R. Lu, S. Liu, C. Wang, A. Yamakata, C. Su, B. Liu, T. Ohno, Atomically dispersed antimony on carbon nitride for the artificial photosynthesis of hydrogen peroxide, Nat. Catal. 4 (2021) 374–384.
[35] Z. Yu, Y. Li, A. Torres-Pinto, A.P. LaGrow, V.M. Diaconescu, L. Simonelli, M.J. Sampaio, O. Bondarchuk, I. Amorim, A. Araujo, A.M.T. Silva, C.G. Silva, J.L. Faria, L. Liu, Single-atom Ir and Ru anchored on graphitic carbon nitride for efficient and stable electrocatalytic/photocatalytic hydrogen evolution, Appl. Catal. B Environ. 310 (2022) 121318.
[36] X. Liu, S. Ye, G. Lan, P. Su, X. Zhang, C.A.H. Price, Y. Li, J. Liu, Atomic pyridinic nitrogen sites promoting levulinic acid hydrogenations over double-shelled hollow Ru/C nanoreactors, Small 17 (2021) 2101271.
[37] J. Deng, C. Zhou, Y. Yang, B. Nan, L. Dong, L. Cai, L. Li, Z.-J. Wang, X. Yang, Z. Chen, Visible-light-driven selective cleavage of C-C bonds in lignin model substrates using carbon nitride-supported ruthenium single-atom catalyst, Chem. Eng. J. 462 (2023), 142282.
[38] L. Du, Q. Tian, X. Zheng, W. Guo, W. Liu, Y. Zhou, F. Shi, Q. Xu, Supercritical CO_2-tailored 2D oxygen-doped amorphous carbon nitride for enhanced photocatalytic activity, Energy Environ. Mater. 5 (2022) 912–917.
[39] Y. Wu, R. Yao, Q. Zhao, J. Li, G. Liu, La-RuO_2 nanocrystals with efficient electrocatalytic activity for overall water splitting in acidic media: synergistic effect of La doping and oxygen vacancy, Chem. Eng. J. 439 (2022), 135699.
[40] X. Liu, Z. Hao, H. Wang, T. Wang, Z. Shen, H. Zhang, S. Zhan, J. Gong, Enhanced localized dipole of Pt-Au single-site catalyst for solar water splitting, Proc. Natl. Acad. Sci. 119 (2022), e2119723119.

[41] Q. Liu, H. Cheng, T. Chen, T.W.B. Lo, J. Ma, A. Ling, F. Wang, Boosted CO desorption behaviors induced by spatial dyadic heterostructure in polymeric carbon nitride for efficient photocatalytic CO_2 conversion, Appl. Catal. B Environ. 295 (2021), 120289.

[42] Q. You, C. Zhang, M. Cao, B. Wang, J. Huang, Y. Wang, S. Deng, G. Yu, Defects controlling, elements doping, and crystallinity improving triple-strategy modified carbon nitride for efficient photocatalytic diclofenac degradation and H_2O_2 production, Appl. Catal. B Environ. 321 (2023), 121941.

[43] W. Liu, L. Cao, W. Cheng, Y. Cao, X. Liu, W. Zhang, X. Mou, L. Jin, X. Zheng, W. Che, Q. Liu, T. Yao, S. Wei, Single-site active cobalt-based photocatalyst with a long carrier lifetime for spontaneous overall water splitting, Angew. Chem. Int. Ed. 56 (2017) 9312–9317.

[44] K. Liu, J. Ma, X. Yang, D. Jin, Y. Li, G. Jiao, S. Yao, S. Sun, R. Sun, Boosting electron kinetics of anatase TiO_2 with carbon nanosheet for efficient photo-reforming of xylose into biomass-derived organic acids, J. Alloy. Compd. 906 (2022), 164276.

[45] E. Wang, A. Mahmood, S.-G. Chen, W. Sun, T. Muhmood, X. Yang, Z. Chen, Solar-driven photocatalytic reforming of lignocellulose into H_2 and value-added biochemicals, ACS Catal. 12 (2022) 11206–11215.

[46] R. Das, S. Sarkar, R. Kumar, S. D. Ramarao, A. Cherevotan, M. Jasil, C.P. Vinod, A. K. Singh, S.C. Peter, Noble-metal-free heterojunction photocatalyst for selective CO_2 reduction to methane upon induced strain relaxation, ACS Catal. 12 (2022) 687–697.

[47] J. Ma, Y. Li, D. Jin, X. Yang, G. Jiao, K. Liu, S. Sun, J. Zhou, R. Sun, Reasonable regulation of carbon/nitride ratio in carbon nitride for efficient photocatalytic reforming of biomass-derived feedstocks to lactic acid, Appl. Catal. B Environ. 299 (2021), 120698.

[48] J. Wang, Y. Wang, M. Yu, G. Li, S. Zhang, Q. Zhong, Formation of flaky carbon nitride and beta-Indium sulfide heterojunction with efficient separation of charge carriers for enhanced photocatalytic carbon dioxide reduction, J. Colloid Interface Sci. 611 (2022) 71–81.

[49] J. Hu, T. Yang, X. Yang, J. Qu, Y. Cai, C.M. Li, Highly selective and efficient solar-light-driven CO_2 conversion with an ambient-stable 2D/2D Co_2P@BP/g-C_3N_4 heterojunction, Small 18 (2022) 2105376.

[50] Q. Tang, Z. Sun, S. Deng, H. Wang, Z. Wu, Decorating g-C_3N_4 with alkalinized Ti_3C_2 MXene for promoted photocatalytic CO_2 reduction performance, J. Colloid Interface Sci. 564 (2020) 406–417.

[51] Y. Wang, X. Bai, H. Qin, F. Wang, Y. Li, X. Li, S. Kang, Y. Zuo, L. Cui, Facile one-step synthesis of hybrid graphitic carbon nitride and carbon composites as high-performance catalysts for CO_2 photocatalytic conversion, ACS Appl. Mater. Interfaces 8 (2016) 17212–17219.

[52] Q. Song, Y. Zhou, J. Hu, C. Zhou, X. Shi, D. Li, D. Jiang, Synergistic effects of surface Lewis Base/Acid and nitrogen defect in MgAl layered double Oxides/Carbon nitride heterojunction for efficient photoreduction of carbon dioxide, Appl. Surf. Sci. 563 (2021), 150369.

[53] X. Cheng, J. Wang, K. Zhao, Y. Bi, Spatially confined iron single-atom and potassium ion in carbon nitride toward efficient CO_2 reduction, Appl. Catal. B Environ. 316 (2022), 121643.

[54] J. Wang, Y. Wang, G. Li, Y. Xiong, M. Zhang, S. Zhang, Q. Zhong, Sodium doped flaky carbon nitride with nitrogen defects for enhanced photoreduction carbon dioxide activity, J. Colloid Interface Sci. 603 (2021) 210–219.

[55] Z. Liu, J. Liang, Q. Song, Y. Li, Z. Zhang, M. Zhou, W. Wei, H. Xu, C.-S. Lee, H. Li, Z. Jiang, Construction atomic-level N-P charge transfer channel for boosted CO_2 photoreduction, Appl. Catal. B Environ. 328 (2023), 122472.

[56] L. Wang, B. Cheng, L. Zhang, J. Yu, In situ irradiated XPS investigation on S-scheme TiO_2@$ZnIn_2S_4$ photocatalyst for efficient photocatalytic CO_2 reduction, Small. 17 (2021), 2103447.

[57] J. Ma, D. Jin, Y. Li, D. Xiao, G. Jiao, Q. Liu, Y. Guo, L. Xiao, X. Chen, X. Li, J. Zhou, R. Sun, Photocatalytic conversion of biomass-based monosaccharides to lactic acid by ultrathin porous oxygen doped carbon nitride, Appl. Catal. B Environ. 283 (2021), 119520.

[58] Y. Zhang, H. Luo, L. Kong, X. Zhao, G. Miao, L. Zhu, S. Li, Y. Sun, Highly efficient production of lactic acid from xylose using Sn-beta catalysts, Green Chem. 22 (2020) 7333–7336.

[59] H. Zhou, M. Wang, F. Wang, Oxygen-controlled photo-reforming of biopolyols to CO over Z-scheme CdS@g-C_3N_4, Chem 8 (2022) 465–479.

[60] M. Wang, M. Liu, J. Lu, F. Wang, Photo splitting of bio-polyols and sugars to methanol and syngas, Nat. Commun. 11 (2020) 1083.

[61] Z. Liu, J. Ma, M. Hong, R. Sun, Potassium and sulfur dual sites on highly crystalline carbon nitride for photocatalytic biorefinery and CO_2 reduction, ACS Catal. 13 (2023) 2106–2117.